Advanced Energy and Sustainability Research

ADVANCED ENERGY & SUSTAINABILITY RESEARCH Open Access

www.advenergysustres.com

RESEARCH ARTICLE OPEN ACCESS

Enhancing Lithium-Metal Battery Safety and Performance with Ether-Aided Ionic Liquid Electrolytes

Ziyuan Lyu[1,2] | Dominik Stępień[1,2] | Thomas Diemant[1,2] | Alessandro Mariani[1,2,3] | Dominic Bresser[1,2,4] | Stefano Passerini[1,2,5]

[1]Helmholtz Institute Ulm (HIU) Electrochemical Energy Storage, Ulm, Germany | [2]Karlsruhe Institute of Technology (KIT), Karlsruhe, Germany | [3]Elettra Sincrotrone Trieste, Basovizza, Trieste, Italy | [4]Ulm University (UUlm), Ulm, Germany | [5]International Electrochemical Energy Storage Research Institute (IEES), School of Energy and Mechanical Engineering, Nanjing Normal University, Nanjing, China

Correspondence: Dominic Bresser (dominic.bresser@kit.edu) | Stefano Passerini (stefano.passerini@kit.edu)

Received: 26 January 2026 | **Revised:** 20 May 2026 | **Accepted:** 2 June 2026

Keywords: battery | electrolyte | ether cosolvent | ionic liquid | lithium metal

ABSTRACT

Electrolytes based on ionic liquids (ILs) are promising alternatives to conventional electrolyte systems due to their appealing properties, including enhanced safety owing to their high thermal stability and nonflammability, as well as their superior compatibility with lithium metal. However, their high viscosity limits Li-ion mobility. To overcome this challenge, we developed a dual-anion IL electrolyte incorporating an ether-type cosolvent. This electrolyte combines *N*-butyl-*N*-methylpyrrolidinium bis(fluorosulfonyl)imide ($PYR_{14}FSI$), lithium bis(trifluoromethanesulfonyl)imide (LiTFSI), and 1,2-dimethoxyethane (DME). The incorporation of DME into the electrolyte, $Pyr_{14}FSI$ + LiTFSI 8:2 + x wt.% DME (x = 10, 20, 30, 40), results in an improved Li-ion mobility and promotes the formation of a more stable solid electrolyte interphase, facilitated by the DME-induced decomposition of the FSI^- and $TFSI^-$ anions. Our findings suggest that the addition of 20 wt.% of DME allows for the optimum balance between improved transport properties owing to the presence of DME and high thermal stability thanks to the presence of the IL. This optimized electrolyte yields very stable long-term cycling of Li||NCM622 cells, along with a substantially higher capacity compared to the neat IL electrolyte, thus providing a viable approach to overcome the remaining challenges of IL-based electrolytes, while maintaining their intrinsic advantages.

1 | Introduction

The emergence of lithium-ion batteries (LIBs) revolutionized the energy storage landscape, enabling their widespread utilization in portable devices, electric vehicles, and various other applications since their comercialization in the 1990s [1, 2]. With the growing demand for higher-capacity portable devices and stricter requirements on volume and weight, coupled with graphite nearing its theoretical capacity limits in LIBs (i.e., 372 mAh g^{-1}), the search for alternative anode materials has become imperative [3–5]. Therefore, a new anode material is a must, and the lithium-metal electrode is considered the "holy grail" for the next generation of high-energy density batteries. As lithium metal exhibits an exceptionally low electrochemical potential (−3.040 vs. the standard hydrogen electrode) and high specific capacity (3860 mAh g^{-1}), it has the capability to surpass graphite by a factor of about ten [4, 6].

However, the development of lithium-metal batteries (LMBs) is hindered by several challenges, which are limiting the large-scale development. These include the high reactivity of lithium metal, which leads to the formation of an unstable solid electrolyte interphase (SEI) [4, 6–8], and accelerated lithium dendrite growth, resulting in poor cycle ability and rapid capacity fading [9, 10]. Moreover, the reactivity of lithium metal with commercially used carbonate-based solvents for electrolytes,

such as EC, DEC, and dimethyl carbonate (DMC), does not only lead to severe electrolyte decomposition, but also promotes dendrite formation during cycling [11]. Furthermore, these carbonate-based electrolytes are volatile and flammable, severely limiting their application in LMBs [12–15]. To address these challenges, it is crucial to develop electrolytes with a chemically and electrochemically stable SEI enabling high Coulombic efficiency (CE) and enhancing lithium anode safety [16–18]. ILs have garnered significant attention for their unique properties, including high thermal stability, nonflammability, negligible vapor pressure, and robust SEI formation, making them highly desirable for safer LMBs [16, 17, 19–22]. A unique feature of ILs is that they can be tailored by combining various anions and cations, offering a wide range of design possibilities.

ILs based on pyrrolidinium cations have been reported to exhibit much higher cathodic stability limit, exceeding 5 V versus Li^+/Li, in comparison to most organic solvents [20, 23–26]. In this work, a dual-anion based electrolyte of FSI^- and $TFSI^-$ was chosen. The benefit of utilizing both anions is, on the one hand, that the $TFSI^-$ anion improves the thermal stability and the compatibility with the Li metal anode, displaying more stability than FSI^- [22]. On the other hand, FSI^- inhibits Al current collector corrosion, particularly at high concentrations [27]. The FSI^- anion has also gained attention due to its reduced steric hindrance, leading to lower viscosities and higher ionic conductivities of the electrolyte. The combination of these two imide anions in ionic liquids allows for a balanced combination of conductivity and stability of the electrolyte [22]. A study by Wu et al. [28] employed the dual-anion ionic liquid electrolyte ($0.8PYR_{14}FSI$-0.2LiTFSI; ILE), enabling long-term cycling of nickel-rich cathode materials (NCM88|ILE|Li metal) and achieving 88% capacity retention after 1000 cycles. This notable stability can be attributed to the formation of an exceptionally stable cathode electrolyte interphase (CEI), composed of LiF and S-containing species, facilitated by the IL-based electrolyte [28].

Although the dual anion IL-based electrolyte offers several advantages, it still suffers from relatively high viscosity and low ionic conductivity, due to the strong ionic interactions, especially for the high charge density Li^+ ion [11]. To address these issues, the incorporation of a cosolvent or diluent emerges as a practical solution to decrease viscosity, establishing a hybrid electrolyte system [29].

Previous studies have indicated that ether-based electrolytes, commonly employed in high-energy lithium-sulfur and lithium-air battery systems, exhibit superior performance compared to other organic solvents [30, 31]. This superiority is attributed to the formation of flexible oligomers within the SEI on the lithium anode [32, 33]. Among various ether-based solvents, 1,2-dimethoxyethane (DME) has shown great potential due to its short ether structure backbone and good dissolution of Li^+ ions [33]. Additionally, DME has the lowest reduction potential (1.68 V vs. Li^+/Li) and a relatively wide electrochemical stability window (4.3 V vs. Li^+/Li) compared to other linear ethers [34]. DME was successfully employed as a cosolvent in highly concentrated single-anion IL-based electrolytes (e.g., 3.2 mol kg^{-1} LiFSI in $PYR_{13}FSI$), where it substantially improved Li^+ transport and enabled stable cell cycling [11, 35]. However, pure FSI-based systems can present challenges related to aluminum current collector corrosion at elevated voltages [36, 37], and the use of DME introduces significant safety risks due to its high flammability and volatility, particularly at elevated temperatures [29]. Hence, the amount of DME in the electrolyte needs to be carefully controlled to maintain the unique safety properties offered by IL-based electrolyte systems.

This study focuses on the effect of a gradual change of the weight percentage of DME in a promising dual salt IL-based electrolyte: $Pyr_{14}FSI$ + LiTFSI 8:2 + x wt.% DME (x = 10, 20, 30, 40), with a particular emphasis on the trade-off between improved transport properties and the preservation of safety. The electrolyte mixtures are named in the following as: IL, IL-10DME, IL-20DME, IL-30DME, and IL-40DME. A comprehensive analysis of the physicochemical and electrochemical properties, as well as molecular dynamics (MD) simulations, were employed to optimize the DME composition. Li stripping/plating tests combined with scanning electron microscopy (SEM) and X-ray photoelectron spectroscopy (XPS) were used to investigate the cycling performance and interfacial chemistry at the Li-metal anode. Finally, the optimized composition enabled stable cycling in Li||NCM622 cells, even under lean lithium and electrolyte conditions.

2 | Materials and Methods

2.1 | Preparation of the Hybrid Electrolyte

N-Methylpyrrolidone (Acros Organics) and 1-bromobutane (Merck, 98%) were used for the synthesis of the IL after distillation under atmospheric pressure. Lithium bis(fluorosulfonyl)imide (LiFSI; Provisco, 98%) was dried for 12 h at 80°C under vacuum (10^{-3} bar). The *N*-butyl-*N*-methylpyrrolidinium bis(fluorosulfonyl)imide ($PYR_{14}FSI$) ionic liquid employed in this study was synthesized and purified according to the procedure reported by Montanino et al. [38–40]

The purified $PYR_{14}FSI$ was predried under vacuum at 10^{-3} mbar (in a dry room) and then dried using a turbomolecular pump at 10^{-7} mbar and 20°C for 2 h, then at 50°C for 6 h and, finally, at 80°C for 12 h. Lithium bis(trifluoromethanesulfonyl)imide (LiTFSI; 3 M, battery grade) was dried using a turbomolecular pump at 10^{-7} mbar and 120°C for 12 h, and mixed with the dried IL. The mixtures of the IL and Li salt were dried again at 10^{-7} mbar and 80°C for 12 h. The IL-Li salt mixtures and molecular sieve-dried DME (moisture < 10 ppm) were mixed in various weight ratios starting from 100:0, 90:10, 80:20, and 70:30 to 60:40 (IL:DME).

To keep the salt concentration of LiTFSI constant at 0.775 mol kg^{-1}, matching the standard IL-based electrolyte ($PYR_{14}FSI$ + LiTFSI 8:2 molar ratio), extra LiTFSI was added to compensate for the DME addition. The solutions were stirred at room temperature for 4 h. All the hybrid electrolytes were stored in argon-filled bottles for further usage.

2.2 | Electrode Preparation and Cell Assembly

A slurry of 92 wt.% $LiNi_{0.6}Co_{0.2}Mn_{0.2}O_2$ (NCM622; BASF) as the active material, 4 wt.% of Super C65 (Imerys) as conductive

carbon and 4 wt.% of PVdF (Solvay 5130) as binder were coated on a 15 μm thick Al foil with a wet film thickness of either 60 or 100 μm. The coated Al foils were predried at 80°C in an oven (Binder) for 12 h. After punching electrodes with a diameter of 12 mm, the cathodes were further dried at 10^{-3} mbar and 120°C for 12 h. Subsequently, the electrodes were weighed. The resulting cathode mass loading was around 2.5 ± 0.1 mg cm^{-2} and 5.0 ± 0.1 mg cm^{-2} for the wet coating thicknesses mentioned above. Finally, the electrodes were pressed at 8 t cm^{-2}.

All the electrochemical characterization experiments were conducted using pouch cells that were assembled in a dry room (dew point of the incoming air: < −70°C). Two pieces of 10×10 cm [2] pouch foil, including a nickel and aluminum current collector stripe (Welcos), were used for the cell assembly; for the symmetric Li||Li cells, both current collectors consisted of nickel foil. Lithium-metal foil (Honjo, battery grade) with a thickness of 300 μm was used as electrode (diameter 12 mm) and a glass fiber sheet (Whatman, GF/A) was used as separator if not stated differently. The porous separator was initially soaked in one of the electrolytes (commonly, 100 μL), and subsequently subjected to vacuum (1 mbar for 99 s) in the sealing machine to enhance wetting. Two Li metal electrode foils were then connected with nickel current collectors (Welcos). Before sealing the final open side, the cells were once again subjected to a vacuum step ensuring optimal electrolyte distribution and minimizing the presence of any trapped air within the cell.

2.3 | Physicochemical Characterization

The density of the electrolytes was measured using an Anton Paar DSA5000M density meter. The measurements were conducted in the temperature range from 20°C to 60°C, with a step size of 5°C. The viscosity of the electrolytes was measured using an Anton Paar MCR102 rheometer with a cone-plate geometry with a constant shear rate of 100 s^{-1}. The measurements were conducted in the temperature range from 20°C to 80°C with a step size of 10°C. To assess the wettability, a comparative analysis was conducted by observing the size of liquid droplets on a consistent separator material (Asahi SV718). Droplets containing an equal volume of electrolyte (10 μL) were carefully placed onto the surface of the Asahi separator. After 2 min from the time of droplet deposition, an image was captured.

The ionic conductivity was determined using an automated multiplexed conductivity meter (MCS-10, MMates), equipped with a frequency analyzer and a thermostatic chamber. Sealed glass conductivity cells equipped with two platinized platinum electrodes were employed for the measurements. Prior to each measurement, the conductivity cells were calibrated, and their deviation constants were determined using a 0.01 M aqueous KCl standard solution. The investigated electrolytes were then loaded into the conductivity cells in the dry room. The conductivity of the electrolytes was investigated in the temperature range from −20°C to 60°C, with a step size of 10°C. To ensure equilibrium, the samples were allowed to stabilize for 15 min before acquiring the conductivity measurements. The measurements were recorded over a period of 45 min.

In order to analyze the thermal stability and volatility of the electrolytes, a thermogravimetric analyzer (NETZSCH TG209) was employed, and measurements were conducted under a N_2 atmosphere. The analysis involved loading the electrolyte into an aluminum crucible with ca. 5 mg loading. Using the dynamic TGA mode, the mass loss was recorded against temperature in a heating range from 40°C to 600°C with a temperature ramp of 5°C min^{-1}. For the flammability test, the hybrid electrolytes were placed on a glass plate. The samples were heated/ignited by a jet-flame torch (Leifheit 3084).

2.4 | Electrochemical Characterization

The stripping and plating experiments were performed in symmetric Li||Li pouch cells utilizing a battery tester (BioLogic VMP3B-10). The cells were first thermally equilibrated at a temperature of 20°C for 6 h. Subsequently, a constant current of ±0.272 mA cm^{-2} was applied, which corresponds to ca. 30% of the limiting current density of $PYR_{14}FSI$ + LiTFSI (molar ratio of 8:2). Each stripping/plating step lasted for 1 h and 200 consecutive stripping/plating cycles were performed for all investigated electrolytes.

The limiting current density for the IL electrolyte was measured in symmetric Li||Li cells. The measurement was performed with a sweep rate of 0.01 mV s^{-1} (Solartron Analytical 1287). During the measurements, the current initially increases as the scanning voltage ramps up before reaching a plateau. The intercept of the final current plateau with the *y*-axis was used for estimating the limiting current density.

Electrochemical impedance spectroscopy (EIS) was performed (Biologic VMP3B-10) for every 50th cycle during the lithium stripping/plating tests to monitor changes in resistance at the electrodes. The fitting was performed using the RelaxIS software. R_{Ohm} is given by Z(f) at high frequencies from 1 MHz to 10 kHz. The impedance related to the charge transfer R_{CT} and interface layer R_{SEI} was determined in the medium frequency range from 10 Hz to 10 kHz. To fit the results of this experiment, R_{SEI} and R_{CT} were separated at a frequency of 17,600 Hz. The slow process related to the mass transport is represented in the low frequency range from 10 to 10 mHz [41, 42].

To assess the anodic stability of the electrolytes, Li||Al–C pouch cells were employed, for which an aluminum foil was coated with Super C65 (Imerys). The evaluation was performed using linear sweep voltammetry (Biologic VMP3B-10). The cell voltage was linearly swept at 0.1 mV s^{-1} from OCV to 6.0 V. The anodic stability limit of the electrolyte was determined by the specific voltage at which the current density of the sample reached 10 μA cm^{-2}.

Galvanostatic cycling of Li||NCM622 pouch cells using an NCM622 cathode as the working electrode and lithium metal as the counter electrode was performed on a battery tester (Maccor 4300). The cycling tests were carried out at 20°C in a climatic chamber (Binder). For the C-rate test, the cells initially underwent a rest period at 20°C for 12 h. Subsequently, the cells were cycled using a dis-/charge rate of C/10 for the first five cycles, followed by additional cycles at C/5, C/2, and 1C. Each

C-rate was applied for 5 cycles. Afterward, the cells resumed constant long-term cycling at 0.5 C for 200 cycles. For the long-term cycling test, the cells were cycled at 0.1 C for two (formation) cycles and then at 0.5 C. For an evaluation of the cell performance in practical cells, a thinner lithium metal anode (50 µm, battery grade, Honjo) and separator (Asahi SV718) were used along with a reduced amount of electrolyte (20 µL). The cut-off voltages were set to 4.2 and 2.8 V, and a dis-/charge rate of 1C corresponds to a specific current of 200 mA g^{-1}.

2.5 | Ex Situ Characterization

SEM (ZEISS Crossbeam XB340) was used to investigate the morphology of the electrodes. In addition, an energy-dispersive X-ray detector (EDX; Oxford) was utilized to evaluate the elemental composition. XPS was performed using a PHI 5800 Multi Technique ESCA System. All XPS data were calibrated to the signal of amorphous carbon at 284.9 eV. The peak deconvolution was done using the CasaXPS software. For both SEM-EDX and XPS, the samples recovered from cycled cells were thoroughly washed with DMC to remove residual bulk electrolyte salts, following established protocols for ionic liquid-based systems [28, 43]. The samples were then dried and transferred to the instruments under an argon atmosphere using air-tight transfer boxes.

2.6 | Computational Calculations

MD simulations were carried out using the Amber 18 software exploiting the GAFF force field [44]. The atomic partial charges were obtained with the RESP algorithm from density functional theory (DFT) calculations run with Gaussian09e at the B3LYP/6-311++G** level of theory. The starting random molecular arrangements were obtained by Packmol [45]. The simulation went through different steps, starting from geometrical relaxation, followed by gradual heating of the system from 0 to 50 K in several NVT sessions. The systems were then equilibrated at 300 K for 20 ns in the NPT ensemble, and for a further 20 ns in the NVT ensemble. A final productive NVT phase of 10 ns was then used for the analysis. For the productive phase, the time step used was 2 fs, and the simulation was saved every 1000 steps, obtaining a final trajectory of 5000 frames spaced by 2 ps each. In order to account for charge transfer and polarization effects, the atomic charges of the ionic species were scaled by a factor of 0.74, which is known to yield reliable results for ionic liquids [46].

3 | Results and Discussion

3.1 | Electrolyte Properties and Coordination Structure

Understanding transport properties in ionic liquid-based electrolytes is vital, as strong Coulomb interactions lead to high viscosities, hindering high-mass loadings and charge rates, especially at lower temperatures [22]. To address this, we explored the introduction of a low-viscosity cosolvent, which significantly affects ion mobility and, consequently, conductivity [47]. As shown in Figure 1a,b, the electrolyte $PYR_{14}FSI$ + LiTFSI 8:2 (hereinafter simply referred to as IL) exhibits high viscosity (122 mPa·s) and low conductivity (2.1 mS cm^{-1}) at 20°C. However, upon addition of an increasing DME content, i.e., $PYR_{14}FSI$ + LiTFSI 8:2 + x wt.% DME (x = 10, 20, 30, 40; hereinafter referred to as IL-xDME), the conductivity at 20°C progressively increases from 3.5 to 5.4 mS cm^{-1}, 7.2, and 9.3 mS cm^{-1}, respectively (see Figure 1a). The conductivity increase is more pronounced at lower temperatures, particularly when going from IL-20DME to IL-40DME. This difference is mainly attributed to the lower melting point (−58°C vs. −18°C) and overall lower viscosity of DME in comparison to $PYR_{14}FSI$ [48]. On the other hand, a lesser increase of conductivity is observed at high temperatures, resulting from the converging viscosity of the electrolytes due to the decreased effect of Coulomb interaction.

The addition of DME has been reported to facilitate the dilution of ionic species and the breaking of Li-FSI/TFSI aggregates, resulting in an increased conductivity [11]. Moreover, DME does not only reduce the viscosity but also improves the wettability, aiding faster electrolyte permeation by easily wetting the commercial PP/PE separator with a smaller pore size. To qualitatively compare the wettability, the droplet size on the separator was examined (Figure S1). A poor wetting of the separator may lead to an uneven distribution of the electrolyte, slowing and/or unevenly distributing the Li^+ flux, and it simply requires more time during the cell fabrication. And, indeed, increasing the DME content results in larger droplets, wider diffusion traces, and larger contact angles, indicating an improved separator wetting [49]. This reduces the time needed for the electrolyte to fill the porous voids, enabling less porous separators, as well as thicker cathodes. Finally, the electrolyte density (Figure S2) decreases with increasing DME content, resulting in a lower weight contribution of this nonactive component.

The anodic electrochemical stability of the electrolyte is critical for batteries utilizing high-voltage cathode materials [50]. As shown in Figure 1c, the linear sweep voltammetry experiments indicate a good stability against conductive carbon coated aluminum current collectors up to at least 4.5 V for all electrolytes. Although the hybrid electrolytes show more side reactions starting from 4.2 V with an increasing DME content, the current density still remains below the 10 µA cm^{-2} threshold. The neat IL electrolyte exceeds 5.0 V, consistent with previous results [51].

While the IL-based electrolytes offer high thermal stability and safety, the inclusion of DME, a solvent with a boiling point of 85°C and a flashpoint of −2°C under atmospheric pressure, introduces fire risks [52]. To evaluate these risks, TGA and flame-exposure tests were conducted (Figure 1d–e). The IL electrolyte demonstrated a high thermal stability up to ~300°C, with LiTFSI stabilizing the FSI^- anion and suppressing its decomposition (Figure 1d and Figure S3). Additionally, the IL could also reduce the evaporation/decomposition rate of the hybrid electrolyte, especially with lower DME content. In a flammability test (Figure 1e), IL-10DME and IL-20DME exhibited self-extinguishing characteristics even upon prolonged exposure to the torch fire. In contrast, IL-30DME and IL-40DME ignited immediately, burning for 7 and 19 s, respectively. The

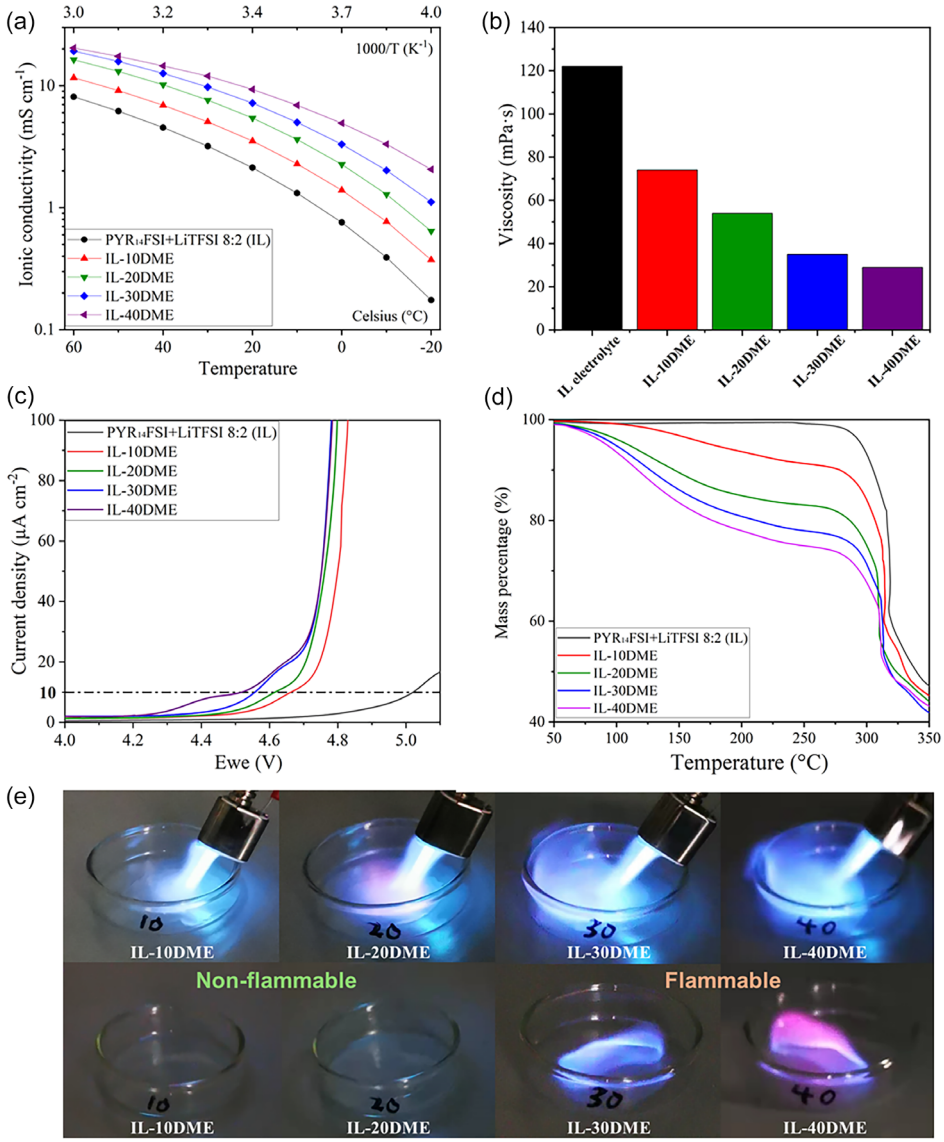

FIGURE 1 | Physicochemical and electrochemical properties of the different electrolyte compositions $PYR_{14}FSI + LiTFSI$ 8:2 + x wt.% DME ($x = 0$, 10, 20, 30, 40; depicted in black, red, green, blue, and violet, respectively): (a) ionic conductivity in the temperature range from −20°C to 60°C; (b) viscosity at 20°C; (c) anodic stability at 20°C versus Super C65 carbon coated Al electrodes at 0.1 mV s^{-1}; (d) thermogravimetric analysis; and (e) flammability tests of electrolytes; in (e) the upper images show the reaction of the electrolytes when subjected to a flame, while the lower images present the behavior after flame removal.

nonvolatility and poor flammability of IL reduce the flame extinction time, greatly enhancing the safety of the electrolyte. Nevertheless, the electrolytes become flammable when the DME content exceeds 20 wt.%.

In ionic liquid-based electrolytes, the formation of Li^+ aggregates takes place due to the strong electrostatic interaction between the Li^+ ions and the anions. DME has a relatively high dielectric constant and a small molecular size. Hence, it easily enters the coordination shell of the Li^+ ions, reducing the binding energy between the cations and anions and, thus, facilitating the dissociation of the lithium salt, and enabling the realization of high salt concentration electrolytes [53]. In fact, DME contains two oxygen atoms in its molecular structure that can act as donor atoms to form a coordination complex with Li-ions [29]. The polar nature of DME facilitates weak hydrogen-bond-like interactions with the imide anions, which helps to suppress the formation of Li-FSI and Li-TFSI aggregates, thus, changing the coordination environment and transport properties of the Li^+ ions [11, 52]. In order to better elucidate the change of the solvation structure in the IL-DME mixed hybrid electrolytes, MD simulations were carried out and compared for IL, IL-20DME, and IL-40DME. In the first step, the coordination number (CN) between Li and O was calculated (Figure 2a). In the neat IL electrolyte, each Li^+ coordinates with between 4 and 5 imide anions with a CN (Li—O) of 0.9 for $TFSI^-$ and 3.6 for FSI^-, respectively. However, the Li^+ coordination sharply changes after the incorporation of DME into the electrolytes. For IL-20DME, 1.2 DME molecules are found in the coordination shell of Li^+, with each DME replacing about 1.5 imide ions (1.2 FSI^- and 0.3 $TFSI^-$). This average value does not imply that every DME molecule in IL-20DME is coordinated. A fraction of the DME is bound to Li^+, while the remainder may be free. When the DME content is further increased to 40 wt.%, the CN of DME,

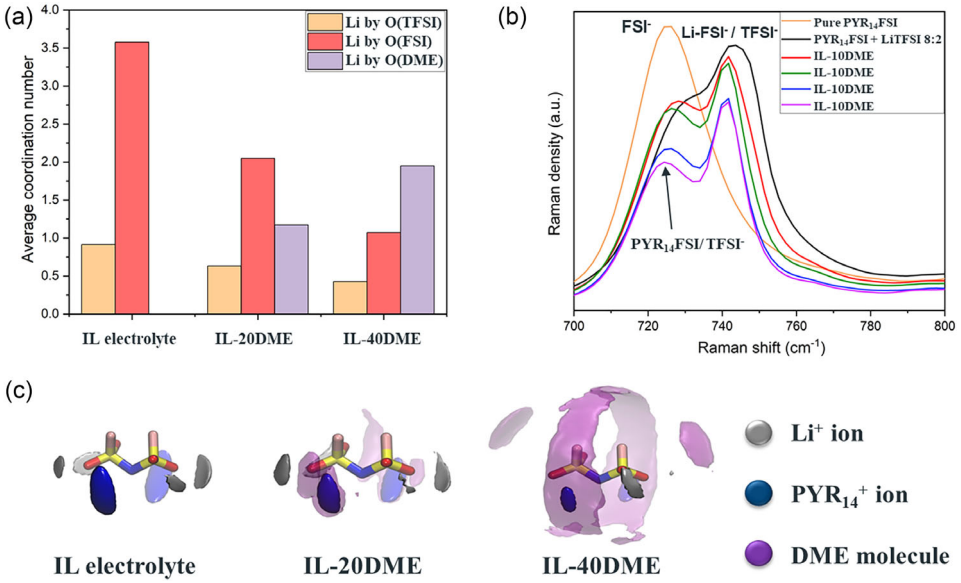

FIGURE 2 | Coordination environment of the different electrolyte compositions $PYR_{14}FSI + LiTFSI$ 8:2 + x wt.% DME ($x = 0$, 10, 20, 30, 40): (a) average coordination number of Li—O (TFSI, orange; FSI, red; and DME, violet) for the electrolytes with a DME content of 0%, 20%, and 40%; (b) Raman spectroscopy data recorded for all the electrolytes at 20°C; and (c) pictorial illustration of the coordination according to MD simulations; the gray, purple, and blue clouds represent the electron clouds of Li^+, Pyr_{14^+}, and DME, respectively.

however, only increases by 0.8. This is lower than the value calculated for IL-20DME, meaning that additional free DME molecules may not be coordinating the Li^+ ions. It appears noteworthy at this stage that free, i.e., uncoordinated solvent molecules have been reported to cause poor lithium plating stripping efficiency [4]. As observed in the Raman analysis (Figure 2b), the addition of DME leads to a shift of the Li-FSI^-/$TFSI^-$ coordination peak from 747 to 743 cm^{-1}. This shift, along with the presence of free FSI^-/$TFSI^-$ anions, indicates that the Li^+ ion coordination structures become hybrid, incorporating both imide anions and DME. This spectroscopic evidence provides hints about the relative amounts of coordinated versus free DME. Figure 2c illustrates the coordination toward the FSI^- of IL mixtures. The gray, blue, and purple clouds represent the electron distribution of Li^+, $PYR_{14}{}^+$, and DME, respectively. It was previously reported that Li^+ and FSI^- can form large ion aggregates in ionic liquid-based electrolytes, since 4 Li^+ are closely coordinated toward the FSI^- anion, see Figure 2c. In the IL-20DME electrolyte, DME molecules are located in between the Li^+ ions and FSI^- anion. According to radial distribution functions (RDFs) for DME, compared to other constituents in the hybrid electrolyte, DME displayed a relatively smaller coordination distance with the Li^+ ions than the imide ions, as depicted in Figure S4. This may indicate that certain parts of the DME molecule possess a greater affinity toward coordinating with Li^+ ions, consequently promoting the disruption of ion aggregates. This would certainly contribute to the enhanced mobility of the Li^+ ions within the hybrid electrolyte systems. It is worth noting that this selective displacement of FSI^- over $TFSI^-$ by DME produces a solvation landscape distinct from that reported for single-anion FSI systems, where the entire anion population competes equivalently with DME for Li^+ coordination [35, 52]. In the IL-40DME electrolyte, the purple cloud, which represents the DME molecules, appears to envelop all the ionic species. This DME cloud suggests the presence of abundant, uncoordinated DME molecules in the electrolyte, which is also consistent with the reduced increase of the CN when going from 20 to 40 wt.% DME. At the same time, the presence of these uncoordinated DME molecules provides an explanation for the increased flammability of the hybrid electrolyte system for higher DME contents.

3.2 | Compatibility of the Electrolytes Toward Lithium Metal

To assess the stability of the interphase and interface between lithium metal and the electrolytes, long-term lithium stripping/plating tests were performed, employing symmetric Li||Li cells. Galvanostatic cycling (see Figure 3a) was conducted at a constant current density of 0.272 mA cm^{-2}, which corresponds to ca. 30% of the limiting current density of the IL electrolyte at 20°C (0.91 $mAcm^{-2}$, Figure S6). At this current density, the diffusion and migration limitation of Li^+ ions in any of the herein investigated electrolytes were not exceeded, ensuring a relatively stable and controlled deposition of lithium metal [54]. In the initial 5–10 cycles, the cells exhibit higher polarization, likely due to the reconstruction of the native, passive layer on Li and the formation of the SEI. This was followed by a decrease in polarization, reaching a relatively steady state, which marks the end of the major SEI build up and the establishment of a more stable interphase on the lithium electrodes [55]. Interestingly, IL and IL-10DME exhibit a significant drop in polarization around the 10^{th} cycle, followed by deviations during the cycling test, suggesting a less stable interphase. In contrast, the other three electrolytes (IL-20DME to IL-40DME) show a smaller decrease in polarization after the initial cycles and maintain a stable polarization profile, suggesting the formation of a more stable, although less conductive, i.e., thicker, SEI. Magnified voltage profiles at the steady state (190–210 h, see

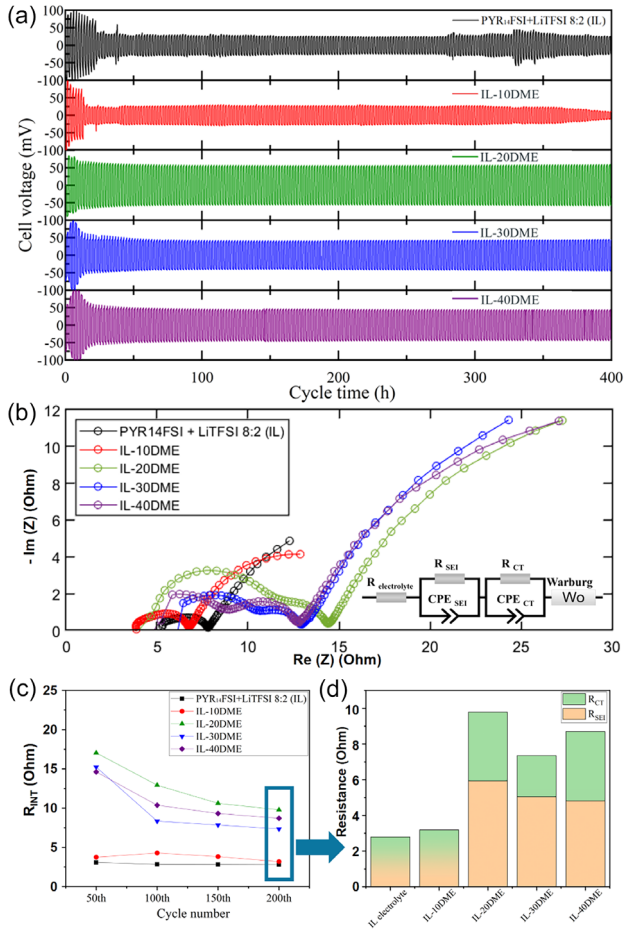

FIGURE 3 | Lithium stripping/plating tests for the electrolyte compositions $PYR_{14}FSI + LiTFSI$ 8:2 + x wt.% DME ($x = 0$, 10, 20, 30, 40; depicted in black, red, green, blue, and violet, respectively). (a) Cell voltage versus time profiles for the lithium stripping/plating tests at a current density of 0.27 mA cm^{-2}; (b) electrochemical impedance spectra displayed as Nyquist plots after the 200th stripping/plating cycle; (c) R_{INT} after the 50th, 100th, 150th, and 200th cycle; and (d) comparison of R_{INT} components after the 200th stripping/plating cycle.

Figure S5) reveal characteristic smooth waveforms with stable overpotentials for all DME-containing electrolytes, indicating highly reversible lithium deposition/dissolution kinetics without microshorting signals [56].

To monitor the evolving interphase, EIS was performed periodically every 50th cycle (see Figure S7) with an equivalent circuit analysis to quantify the interface resistance components [42]. As shown in the representative Nyquist plots at the 200th cycle (Figure 3b), the high-frequency intercepts (R_b) for all electrolytes cluster within the narrow range of 4–6 Ω. It is noted that the vertical drop observed in the ultrahigh frequency region is attributed to the inductive tail from the experimental setup wires, which may mask the precise onset of the bulk resistance but does not affect the determination of the overall resistance magnitude. IL and IL-10DME displayed two depressed and overlapping semicircles throughout cycling, which prevented clear separation of R_{SEI} and R_{CT}, so the total interfacial resistance R_{INT} is reported in Figure 3c. Both electrolytes consistently displayed a low interface resistance, correlating with the low polarization observed in the stripping-plating test, possibly suggesting a comparatively thinner SEI layer. In contrast, IL-20DME, IL-30DME, and IL-40DME showed distinct evolution patterns, displaying a smoother decrease in resistance between the 50th and 100th cycle, followed by an even slower but steady decrease. At any point during the stripping-plating test, the resistance was the highest for IL-20DME, followed by IL-40DME and, finally, IL-30DME. For these electrolytes, the two semicircles corresponding to the interfacial impedance are more evident, enabling a distinction of the contributions. R_{CT} is the component showing the most significant variation among the three electrolytes, acting as the main factor influencing the differing polarization observed in the stripping-plating tests. Nonetheless, R_{SEI} is the dominant component, which may indicate the formation of a thicker and more protective SEI layer during long-term cycling. Besides displaying smaller changes than R_{CT} for the three electrolytes, it shows a different trend, i.e., it decreases for an increasing DME content, as shown in Figure 3d. Rather than simple dilution effects, this trend is likely driven by the modified SEI chemistry. As indicated by the XPS results discussed later, the incorporation of DME promotes the formation of a highly conductive, inorganic-rich (e.g., LiF and Li_3N) interphase, thereby facilitating Li^+ transport across the SEI film [32].

Following the stripping and plating tests, the surface morphology of the lithium-metal electrodes was analyzed via ex situ SEM. In the micrographs presented in Figure 4, no dendrite growth was observed for any of the electrolytes tested. For IL (Figure 4a), the cycled Li metal exhibits a rather dense deposition having small nodular-like deposits that are less than 1 µm in size. With an increasing DME content, the lithium metal morphology becomes more porous. For instance, for IL-10DME and IL-20DME (Figure 4b–c), some network-like or sheet-like particles have been formed. The SEM micrographs of IL-30DME and IL-40DME (Figure 4d–e) display more mossy structures, rendering the surface more porous. The porosity of Li deposits increases the contact area with the electrolyte, leading to active Li loss through decomposition [57]. We may assume that this increased surface area primarily contributes to the observed increase in polarization and R_{INT} for the hybrid electrolytes with a higher DME content (>20 wt.%), while an increased surface area simultaneously also leads to an increased available area for the lithium deposition and charge transfer [58]. Accordingly, there appears to be an "optimum" for which these two effects are balanced, as also apparent from the nonlinear trend concerning the overpotential upon lithium stripping and plating, in fact, revealing the lowest overpotential for IL-30DME (Figure 3c).

3.3 | Analysis of the Electrode/Electrolyte Interphase via XPS

The chemical composition of the SEI formed with the different electrolytes was examined by ex situ XPS after 200 stripping/plating cycles. The results are depicted in Figure 5. Starting with the detail spectra in the C 1s region, four peaks were detected in all spectra at 284.9, 286.3 eV, 288.4, and 289.9 eV, which can be attributed to C—C/C—H, C—N/C—O, C═O, and O—C═O/carbonate species, respectively [28]. The C—C/C—H species are most likely mainly related to C atoms without N coordination

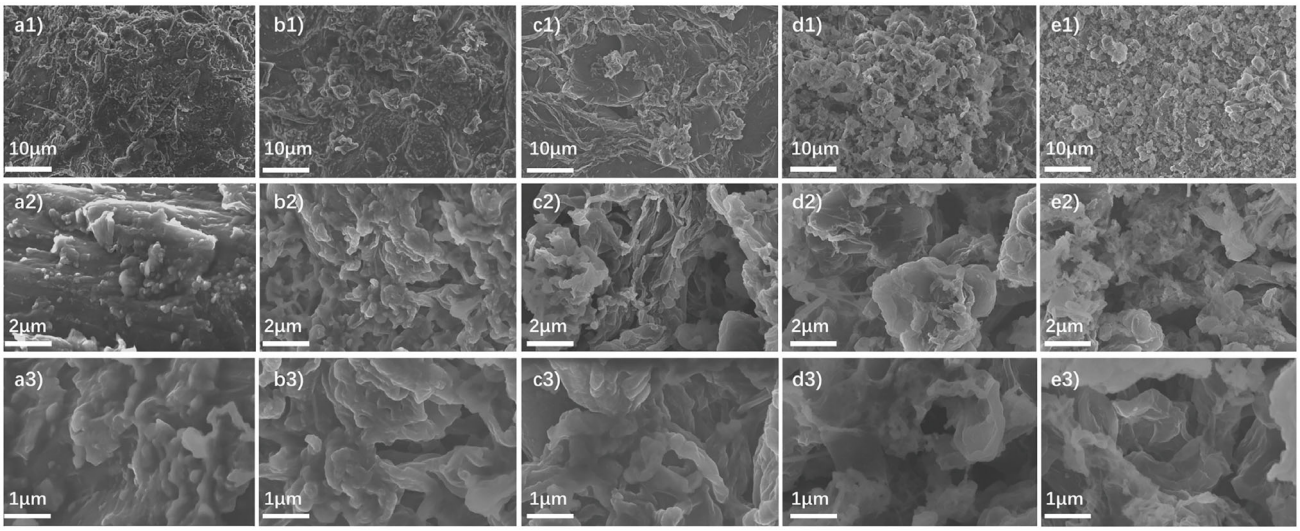

FIGURE 4 | Morphological analysis via SEM of the lithium-metal electrodes after 200 stripping/plating cycles at a current density of 0.27 mA cm^{-2}: (a–e) SEM micrographs for the different electrolyte compositions $PYR_{14}FSI$ + LiTFSI 8:2 (IL) + x wt.% DME (x = 0, 10, 20, 30, and 40; from left to right). The micrographs are arranged with an increasing magnification from top to bottom.

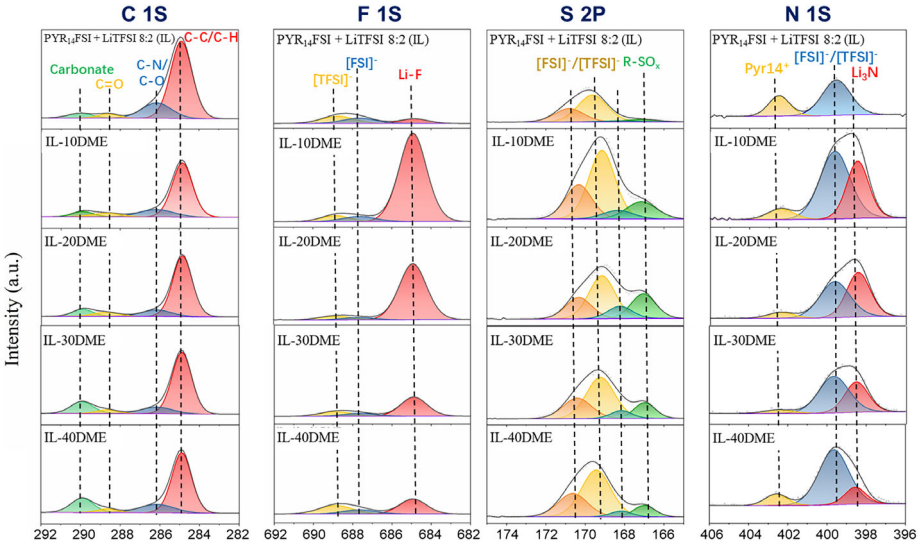

FIGURE 5 | Investigation of the SEI on the lithium-metal electrodes after 200 consecutive lithium stripping/plating cycles at a current density of 0.27 mA cm^{-2} via XPS: detail spectra were obtained for the C 1s, F 1s, S 2p, and N 1s regions (from left to right). The spectra correspond to $PYR_{14}FSI$ + LiTFSI 8:2 (IL) + x wt.% DME (x = 0, 10, 20, 30, and 40; from top to bottom).

in deposited Pyr_{14}^+ or its decomposition products. Correspondingly, C atoms with N coordination in Pyr_{14}^+ should add to the second signal (C—N/C—O) [35]. It is noted that signals at higher binding energies (C═O and O—C═O/carbonate) likely originate from trace DMC solvent residues remaining on the rough surface after the washing step, as well as the native passivation layer (e.g. lithium carbonate) on the lithium foil [59].

In the F 1s spectra, the peak at 684.9 eV, which is attributed to LiF, shows the most significant changes in intensity [60]. This peak exhibits the lowest intensity in the DME-free electrolyte (IL). In contrast, the highest intensity is observed for the electrolyte with 10 wt.% DME. In the following, a declining trend occurs with further increasing DME content, which is likely due to the dilution of FSI^- ions. In fact, LiF is known to be the primary decomposition product of FSI^- [60]. While direct spectroscopic detection of transient radical intermediates is beyond the scope of this work, the increased LiF formation can be rationalized by a synergistic decomposition mechanism supported by literature on analogous ether-based systems. Previous simulations on imide anions (FSI^- and $TFSI^-$) have established that their electrochemical reduction is initiated by S—F and S—N cleavage [61]. Crucially, in electron-rich environments similar to the Li metal interface in this study, these reduction intermediates are reported to trigger the dehydrogenation of DME, forming radical species (e.g., CH_3O^-) [62]. We hypothesize that these reactive species derived from DME may, in turn, lower the kinetic barrier for imide anion decompositions in our hybrid system. This picture is further supported by recent AIMD simulations of imide anion decomposition at lithium metal surfaces [63], as well as

DFT-ReaxFF hybrid studies demonstrating that the initial electron transfer from lithium triggers defluorination and S—N bond cleavage with negligible activation barriers [64]. This proposed pathway aligns well with the experimental XPS results, where the prominent LiF signal coincides with the addition of DME, explaining the formation of a robust, inorganic-rich SEI layer. In addition, the quantitative atomic concentrations extracted from the XPS survey spectra (Figure S8 and Table S1) confirm these trends, showing a marked increase in F content from 2.73 at.% (neat IL) to 11.17 at.% (IL-10DME), followed by a decline to ~3.2 at.% for DME contents exceeding 20 wt.%, consistent with the dilution of FSI^- anions.

Two-peak doublets are detected in the S 2p spectra. The first peak doublet (S $2p_{3/2}$ peak at 169.1 eV) can be assigned to FSI^- and $TFSI^-$ [60]. The other one (S $2p_{3/2}$ peak at 167.1 eV) is related to reduction/decomposition products of the imide anions (RSO_x), mainly formed by cleavage of the S—F bond(s) in the FSI^- anion. The observed species in the S 2p spectra could be essential components of the SEI layer, contributing to its enhanced stability by reinforcing its mechanical properties [60]. It is interesting to note that especially the intensity of the second peak doublet (RSO_x) is much lower for IL than for the electrolytes containing DME.

Moreover, in the N 1s region, the intensity of the Li_3N signal at 398.5 eV follows a similar trend as that observed for LiF. Li_3N in the surface layer of the Li anode is reported to suppress further decomposition of the electrolyte, due to its low electronic and high Li-ion conductivity [32]. In addition, two other signals are detected in the N 1s spectra. The peak at 399.7 eV is associated with pristine FSI^-/TFSI, and the one at 402.3 eV is due to the nitrogen atom in Pyr_{14}^+. As expected, the intensity of the FSI^-/$TFSI^-$ peak in the N 1s spectra follows a similar trend as observed in the S 2p spectra.

The incorporation of larger amounts of LiF and Li_3N is obviously linked to the addition of DME as a cosolvent in the electrolyte, which is probably due to the accelerated decomposition of FSI^-, caused by dehydrogenation products of DME. These species are electronically insulating and have been widely reported to contribute to a more stable interphase [8, 65]. A comprehensive first-principles investigation of the coupled FSI^-/$TFSI^-$/DME decomposition network in this dual-anion system would be a valuable subject for future computational work.

3.4 | Evaluation of the Electrolytes in Li||NCM622 Cells

Finally, we conducted galvanostatic cycling of Li||NCM622 cells using the different electrolytes, as presented in Figure 6. The C-rate test followed by long-term cycling at 0.5 C was carried out employing an NCM622 cathode with an active material mass loading of about 5 mg cm^{-2}, see Figure 6a. The results indicate that cells with a higher DME content provide a higher capacity, particularly at higher C-rates starting from about 0.5 C. The IL-40DME electrolyte shows the highest capacity, exceeding 140 mAh g^{-1} after 200 cycles at 0.5 C, largely surpassing that of IL (only 40 mAh g^{-1}), yielding a capacity retention of 90.5% compared to only 81.2% in the case of IL. This is in good agreement with the comparison of the average CE, being up to 99.92% for the electrolytes containing more than 20 wt.% DME compared to 99.38% for the neat IL (Figure S9). The comparison with galvanostatic cycling data obtained for Li||NCM622 cells containing NCM622 electrodes with a significantly lower active material mass loading of ca. 2.5 mg cm^{-2} (Figure S10), however, unveils that the lower capacity observed for IL stems from insufficient wetting and charge transport limitations, apparently, as all cells independent of the electrolyte, show a very

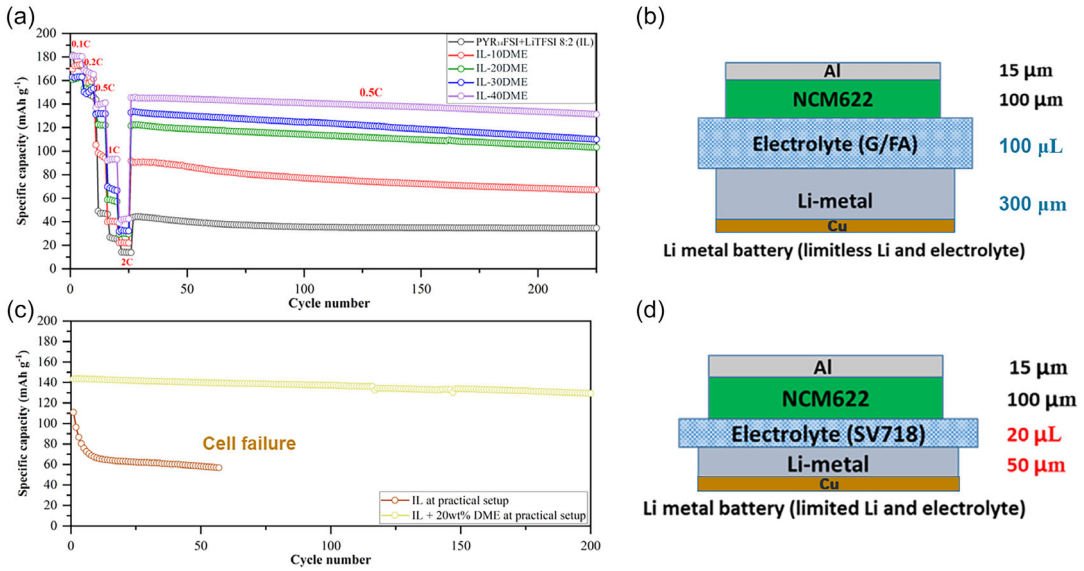

FIGURE 6 | Galvanostatic cycling performance of Li||NCM622 cells employing different electrolyte compositions $PYR_{14}FSI + LiTFSI$ 8:2 + x wt.% DME (x = 0, 10, 20, 30, and 40; depicted in black, red, green, blue, and violet, respectively). (a) Rate capability test conducted in a standard configuration (illustrated in panel b) utilizing a 300 µm Li anode and 100 µL electrolyte. (c) Long-term cycling stability evaluated under constrained conditions (illustrated in panel d) utilizing a thin Li anode (50 µm) and reduced electrolyte volume (20 µL). All cells employ NCM622 cathodes with an active material mass loading of 5.0 mg cm^{-2}.

comparable cycling stability and specific capacity of around 150 mAh g^{-1} after 200 cycles at 0.5 C. A critical factor often overlooked in both cases, however, is the impact of the electrolyte composition on the lithium-metal electrode, as both the electrolyte (100 µL) and lithium metal (300 µm) are present in large excess (Figure 6b). To rigorously evaluate the interfacial durability under more constrained conditions, we also conducted galvanostatic cycling of Li||NCM622 cells containing a much thinner lithium electrode (50 µm) and reduced electrolyte volume of only 20 µL (see Figure 6c,d). Since IL-20DME exhibited the optimal balance between safety features and performance, though, we limited the comparison to this electrolyte composition and neat IL as a reference. Remarkably, the Li||NCM622 cell containing IL as the electrolyte shows rapid capacity fading and fails after only about 60 cycles. This premature failure is attributed not only to the lower CE but primarily to the high viscosity of the neat IL. Under these lean-electrolyte conditions, the poor wettability of the separator limits its wettability, which in turn restricts ion transport and increases polarization. An inhomogeneous Li^+ flux promotes the formation of nonuniform Li deposition, eventually leading to dendrite formation and internal short circuits. In comparison, the capacity of the Li||NCM622 cell containing IL-20DME remained very stable with around 130 mAh g^{-1}, maintaining highly reversible voltage profiles with well-defined plateaus and limited polarization buildup over 200 cycles (Figure S11). These results demonstrate that the incorporation of minor amounts of DME is a very promising approach to benefit from the great advantages of ionic liquid-based electrolytes, while extending such nonflammable electrolyte system into significantly more constrained cell environments, marking a crucial step toward their viability in realistic battery configurations.

To further validate the practical viability of IL-20DME under more demanding conditions, Li||NCM811 cells were fabricated with high-areal-loading cathodes (~9.5 mg cm^{-2}), thin lithium anodes (50 µm), and lean electrolyte (20 µL). As shown in Figure S12a, the cells deliver a stable discharge capacity of ~165–167 mAh g^{-1} at 0.1 C over the initial 10 cycles, with well-defined voltage profiles (Figure S12b) and minimal polarization increase, demonstrating that IL-20DME can support adequate ion transport even through substantially thicker electrodes under lean electrolyte conditions. In addition, the safety advantage of IL-20DME at the battery-component level was confirmed by HP-DSC analysis of charged cathode material (Figure S13). The commercial electrolyte (1M LiPF6 in EC/DMC 1v/1v) exhibits pronounced exothermic peaks at ~200°C and ~220°C, whereas IL-20DME shows a flat thermal response up to 300°C, confirming that the thermal stability of the dual-anion IL matrix is largely preserved with 20 wt.% DME.

4 | Conclusion

In this study, we assessed the performance of hybrid electrolytes comprising $Pyr_{14}FSI$ + LiTFSI 8:2 and varying amounts of DME ranging from 0 to 40 wt.%. The neat IL appeared suboptimal due to its high viscosity, leading to lower conductivity and wettability compared to state-of-the-art liquid electrolytes. To address this limitation, DME was introduced as a low-viscosity cosolvent. Interestingly, the introduction of DME also reduces the formation of Li-imide aggregate structures, which in turn enhances the Li^+ ion dynamics. However, excessive DME content compromise safety due to its volatility and flammability, with the electrolytes becoming notably flammable for DME contents exceeding 20 wt.%. Electrochemically, DME stabilizes the lithium stripping-plating owing to the formation of an LiF- and Li_3N-rich SEI, but also induces the formation of a porous surface, leading to an increased electrolyte decomposition, potentially due to uncoordinated DME molecules, especially above 20 wt.%. At the same time, hybrid electrolytes with a higher DME content exhibit greater capacities and enhanced cycling stability, particularly in configurations closer to practical applications, due to an improved Li^+ ion transport and wetting properties. In summary, the addition of DME is generally favorable for ionic liquid-based electrolytes, though there is an optimum for which the different properties are best balanced: in our case at 20 wt.% DME, yielding a nonflammable, high-performance lithium battery electrolyte. This is further corroborated by HP-DSC measurements confirming a substantially wider thermal safety margin compared to conventional carbonate-based electrolytes, and by proof-of-concept cycling with high-mass-loading NCM811 cathodes (~9.5 mg cm^{-2}) under lean electrolyte conditions. Looking forward, bridging the remaining gap to full commercial viability will require translating these interfacial insights to high-areal-capacity cathodes. Future optimization should focus on fine-tuning the ether/IL ratio specifically for such dense electrode architectures to maintain the delicate balance between viscosity, flammability, and transport kinetics established in this study. In addition, first-principles investigations of the coupled FSI^-/$TFSI^-$/DME decomposition network would provide valuable mechanistic insight into the interphase formation in this dual-anion system.

Author Contributions

Ziyuan Lyu performed the physicochemical and electrochemical characterization and SEM measurements, analyzed all the experimental data, and drafted the manuscript. **Dominik Stępień** conceptualized the activities and revised the manuscript. **Thomas Diemant** performed the XPS measurements, analyzed the data and revised the manuscript. **Alessandro Mariani** performed the molecular dynamics simulations and revised the manuscript. **Dominic Bresser** and **Stefano Passerini** conceptualized and coordinated the activities, provided funding for the work, and revised the manuscript.

Acknowledgments

The authors would like to acknowledge the financial support from the Helmholtz Association and the German Federal Ministry of Education and Research (BMBF), now named the Federal Ministry of Research, Technology and Space (BMFTR) within the LILLINT (03XP0225D) and LILLINT-2 project (03XP0511E).

Open Access funding enabled and organized by Projekt DEAL.

Funding

This work was supported by the Bundesministerium für Bildung und Forschung (03XP0225D and 03XP0511E).

Conflicts of Interest

The authors declare no conflicts of interest.

Data Availability Statement

The data that support the findings of this study are available from the corresponding author upon reasonable request.

References

1. M. Armand, P. Axmann, D. Bresser, et al., "Lithium-Ion Batteries – Current State of the Art and Anticipated Developments," *Journal of Power Sources* 479 (2020): 228708, https://doi.org/10.1016/j.jpowsour.2020.228708.

2. W. Li, R. Long, H. Chen, and J. Geng, "A Review of Factors Influencing Consumer Intentions to Adopt Battery Electric Vehicles," *Renewable and Sustainable Energy Reviews* 78 (2017): 318–328, https://doi.org/10.1016/j.rser.2017.04.076.

3. J. B. Goodenough and K. S. Park, "The Li-Ion Rechargeable Battery: A Perspective," *Journal of the American Chemical Society* 135, no. 4 (2013): 1167–1176, https://doi.org/10.1021/ja3091438.

4. J. Qian, W. A. Henderson, W. Xu, et al., "High Rate and Stable Cycling of Lithium Metal Anode," *Nature Communications* 6 (2015): 6362, https://doi.org/10.1038/ncomms7362.

5. Z. Chen, D. Bresser, J. Asenbauer, et al., "The success story of graphite as a lithium-ion anode material 02013; fundamentals, remaining challenges, and recent developments including silicon (oxide) composites," *Sustainable Energy & Fuels* 4, no. 11 (2020): 5387–5416, https://doi.org/10.1039/d0se00175a.

6. J. M. Tarascon and M. Armand, "Issues and Challenges Facing Rechargeable Lithium Batteries," *Nature* 414 (2001): 359–367, https://doi.org/10.1038/35104644.

7. J. Qian, B. D. Adams, J. Zheng, et al., "Anode-Free Rechargeable Lithium Metal Batteries," *Advanced Functional Materials* 26, no. 39 (2016): 7094–7102, https://doi.org/10.1002/adfm.201602353.

8. X. He, D. Bresser, S. Passerini, et al., "The Passivity of Lithium Electrodes in Liquid Electrolytes for Secondary Batteries," *Nature Reviews Materials* 6, no. 11 (2021): 1036–1052, https://doi.org/10.1038/s41578-021-00345-5.

9. L. Li, S. Li, and Y. Lu, "Suppression of Dendritic Lithium Growth in Lithium Metal-Based Batteries," *Chemical Communications* 54, no. 50 (2018): 6648–6661, https://doi.org/10.1039/c8cc02280a.

10. C. C. Su, X. Wu, K. Amine, and M. V. Bracamonte, "Probing the Effectiveness in Stabilizing Lithium Metal Anodes through Functional Additives," *ACS Applied Materials & Interfaces* 15, no. 50 (2023): 59016–59024, https://doi.org/10.1021/acsami.3c14119.

11. U. Pal, F. Chen, D. Gyabang, et al., "Enhanced Ion Transport in an Ether Aided Super Concentrated Ionic Liquid Electrolyte for Long-Life Practical Lithium Metal Battery Applications," *Journal of Materials Chemistry A* 8, no. 36 (2020): 18826–18839, https://doi.org/10.1039/d0ta06344d.

12. A. Basile, A. I. Bhatt, and A. P. O'Mullane, "Stabilizing lithium metal using ionic liquids for long-lived batteries," *Nature Communications* 7 (2016): 1–11, https://doi.org/10.1038/ncomms11794.

13. M. A. Navarra, "Ionic liquids as safe electrolyte components for Li-metal and Li-ion batteries," *MRS Bulletin* 38, no. 7 (2013): 548–553, https://doi.org/10.1557/mrs.2013.152.

14. M. Watanabe, M. L. Thomas, S. Zhang, K. Ueno, T. Yasuda, and K. Dokko, "Application of Ionic Liquids to Energy Storage and Conversion Materials and Devices," *Chemical Reviews* 117, no. 10 (2017): 7190–7239, https://doi.org/10.1021/acs.chemrev.6b00504.

15. C. Xu and Z. Cheng, "Thermal Stability of Ionic Liquids: Current Status and Prospects for Future Development," *Processes* 9, no. 2 (2021): 1–36, https://doi.org/10.3390/pr9020337.

16. A. Balducci, "Ionic Liquids in Lithium-Ion Batteries," *Topics in Current Chemistry* 375, no. 2 (2017): 1–27, https://doi.org/10.1007/s41061-017-0109-8.

17. F. Wu, N. Zhu, Y. Bai, L. Liu, H. Zhou, and C. Wu, "Highly Safe Ionic Liquid Electrolytes for Sodium-Ion Battery: Wide Electrochemical Window and Good Thermal Stability," *ACS Applied Materials & Interfaces* 8, no. 33 (2016): 21381–21386, https://doi.org/10.1021/acsami.6b07054.

18. X. He, D. Bresser, S. Passerini, et al., "Strategies towards Enabling Lithium Metal in Batteries: Interphases and Electrodes," *Energy & Environmental Science* 14, no. 10 (2021): 5289–5314, https://doi.org/10.1039/d1ee00767j.

19. L. M. McGrath and J. F. Rohan, "Pyrrolidinium Containing Ionic Liquid Electrolytes for Li-Based Batteries," *Molecules* 25, no. 24 (2020): 6002, https://doi.org/10.3390/molecules25246002.

20. H. De Vries, S. Jeong, and S. Passerini, "Ternary Polymer Electrolytes Incorporating Pyrrolidinium-Imide Ionic Liquids," *RSC Advances* 5 (2015): 13598–13606, https://doi.org/10.1039/c4ra16070c.

21. F. Wu, A. Mullaliu, T. Diemant, et al., "Beneficial Impact of Lithium Bis (Oxalato) Borate as Electrolyte Additive for High-Voltage Nickel-Rich Lithium-Battery Cathodes," *InfoMat* 5 (2023): 1–14, https://doi.org/10.1002/inf2.12462.

22. J. Tong, S. Wu, N. von Solms, et al., "The Effect of Concentration of Lithium Salt on the Structural and Transport Properties of Ionic Liquid-Based Electrolytes," *Frontiers in Chemistry* 7, no. 2020): 1–10, https://doi.org/10.3389/fchem.2019.00945.

23. M. Kerner and P. Johansson, "Pyrrolidinium FSI and TFSI-Based Polymerized Ionic Liquids as Electrolytes for High-Temperature Lithium-Ion Batteries," *Batteries* 4, no. 1 (2018): 10, https://doi.org/10.3390/batteries4010010.

24. M. Kunze, S. Jeong, G. B. Appetecchi, M. Schönhoff, M. Winter, and S. Passerini, "Mixtures of Ionic Liquids for Low Temperature Electrolytes," *Electrochimica Acta* 82 (2012): 69–74, https://doi.org/10.1016/j.electacta.2012.02.035.

25. K. Xue, Z. Zheng, K. Su, X. Zhang, Y. Wang, and J. Lang, "Enhancing Stability in Acetonitrile-Based Supercapacitors : Implementation of Di-Pyrrolidinium Ionic Salts," *Chemical Engineering Journal* 491, no. 2024): 152090, https://doi.org/10.1016/j.cej.2024.152090.

26. A. Santiago-alonso, S. Manuel, and R. S. Emeterio, "Pyrrolidinium-Based Ionic Liquids as Advanced Non-Aqueous Electrolytes for Safer Next Generation Lithium Batteries," *Batteries* 10 (2024): 319.

27. S. Theivaprakasam, G. Girard, P. Howlett, M. Forsyth, S. Mitra, and D. MacFarlane, "Passivation behaviour of aluminium current collector in ionic liquid alkyl carbonate (hybrid) electrolytes," *Npj Materials Degradation* 2, no. 1 (2018): 1–9, https://doi.org/10.1038/s41529-018-0033-6.

28. F. Wu, S. Fang, M. Kuenzel, et al., "Dual-Anion Ionic Liquid Electrolyte Enables Stable Ni-Rich Cathodes in Lithium-Metal Batteries," *Joule* 5, no. 8 (2021): 2177–2194, https://doi.org/10.1016/j.joule.2021.06.014.

29. D. Gyabeng, P. A. Martin, U. Pal, M. Deschamps, M. Forsyth, and L. A. O'Dell, "Investigating Intermolecular Interactions in a DME-Based Hybrid Ionic Liquid Electrolyte by HOESY NMR," *Frontiers in Chemistry* 7, no. 2019): 1–6, https://doi.org/10.3389/fchem.2019.00004.

30. J. Xiang and Y. Lu, "Ether-Based High-Voltage Lithium Metal Batteries: The Road to Commercialization,"*ACS Nano* 18 (2024): 10726–10737, https://doi.org/10.1021/acsnano.4c00110.

31. T. Xu, T. Zheng, Z. Ru, et al., "Ether-Based Electrolyte for High-Temperature and High-Voltage Lithium Metal Batteries," *Advanced*

Functional Materials 34 (2024): 1–11, https://doi.org/10.1002/adfm.202313319.

32. H. Zhang, C. Shen, Y. Huang, and Z. Liu, "Spontaneously Formation of SEI Layers on Lithium Metal from LiFSI/DME and LiTFSI/DME Electrolytes," *Applied Surface Science* 537 (2021): 147983, https://doi.org/10.1016/j.apsusc.2020.147983.

33. Y. Chen, Z. Yu, P. Rudnicki, et al., "Steric Effect Tuned Ion Solvation Enabling Stable Cycling of High-Voltage Lithium Metal Battery," *Journal of the American Chemical Society* 143 (2021): 18703–18713, https://doi.org/10.1021/jacs.1c09006.

34. R. Miao, J. Yang, Z. Xu, J. Wang, Y. Nuli, and L. Sun, "A New Ether-Based Electrolyte for Dendrite-Free Lithium-Metal Based Rechargeable Batteries," *Scientific Reports* 6, no. 1 (2016): 2–10, https://doi.org/10.1038/srep21771.

35. U. Pal, D. Rakov, B. Lu, et al., "Interphase Control for High Performance Lithium Metal Batteries Using Ether Aided Ionic Liquid electrolyte," *Energy & Environmental Science* 15 (2022): 1907–1919, https://doi.org/10.1039/d1ee02929k.

36. C. Luo, Y. Li, W. Sun, et al., "Revisiting the Corrosion Mechanism of LiFSI Based Electrolytes in Lithium Metal Batteries," *Electrochimica Acta* 419 (2022): 140353, https://doi.org/10.1016/j.electacta.2022.140353.

37. A. Abouimrane, J. Ding, and I. J. Davidson, "Liquid Electrolyte Based on Lithium Bis-Fluorosulfonyl Imide Salt: Aluminum Corrosion Studies and Lithium Ion Battery Investigations," *Journal of Power Sources* 189, no. 1 (2009): 693–696, https://doi.org/10.1016/J.JPOWSOUR.2008.08.077.

38. A. Balducci, S. S. Jeong, G. T. Kim, et al., "Development of safe, green and high performance ionic liquids-based batteries (ILLIBATT project)," *Journal of Power Sources* 196, no. 22 (2011): 9719–9730, https://doi.org/10.1016/j.jpowsour.2011.07.058.

39. M. De Francesco, E. Simonetti, G. Gorgi, and G. Appetecchi, "About the Purification Route of Ionic Liquid Precursors," *Challenges* 8, no. 1 (2017): 11, https://doi.org/10.3390/challe8010011.

40. M. Montanino, F. Alessandrini, S. Passerini, and G. B. Appetecchi, "Water-Based Synthesis of Hydrophobic Ionic Liquids for High-Energy Electrochemical Devices," *Electrochimica Acta* 96 (2013): 124–133, https://doi.org/10.1016/j.electacta.2013.02.082.

41. S. Drvarič Talian, J. Bobnar, A. R. Sinigoj, I. Humar, and M. Gaberšček, "Transmission Line Model for Description of the Impedance Response of Li Electrodes with Dendritic Growth," *Journal of Physical Chemistry C* 123, no. 46 (2019): 27997–28007, https://doi.org/10.1021/acs.jpcc.9b05887.

42. W. Choi, H. C. Shin, J. M. Kim, J. Y. Choi, and W. S. Yoon, "Modeling and Applications of Electrochemical Impedance Spectroscopy (Eis) for Lithium-Ion Batteries," *Journal of Electrochemical Science and Technology* 11, no. 1 (2020): 1–13, https://doi.org/10.33961/jecst.2019.00528.

43. D. Stępień, B. Wolff, T. Diemant, et al., "Insights into the Lithium Nucleation and Plating/Stripping Behavior in Ionic Liquid-Based Electrolytes," *ACS Applied Materials & Interfaces* 15, no. 21 (2023): 25462–25472, https://doi.org/10.1021/acsami.3c01722.

44. J. Wang, R. M. Wolf, J. W. Caldwell, P. A. Kollman, and D. A. Case, "Development and Testing of a General Amber Force Field," *Journal of Computational Chemistry* 25 (2004): 1157–1174, https://doi.org/10.1002/jcc.20035.

45. L. Martinez, R. Andrade, E. G. Birgin, and J. M. Martínez, "PACKMOL: A Package for Building Initial Configurations for Molecular Dynamics Simulations," *Journal of Computational Chemistry* 30, no. 13 (2009): 2157–2164, https://doi.org/10.1002/JCC.21224.

46. A. Mariani, R. Caminiti, M. Campetella, and L. Gontrani, "Pressure-Induced Mesoscopic Disorder in Protic Ionic Liquids: First Computational Study," *Physical Chemistry Chemical Physics* 18, no. 4 (2016): 2297–2302, https://doi.org/10.1039/C5CP06800B.

47. A. M. O'Mahony, D. S. Silvester, L. Aldous, C. Hardacre, and R. G. Compton, "Effect of Water on the Electrochemical Window and Potential Limits of Room-Temperature Ionic Liquids," *Journal of Chemical and Engineering Data* 53, no. 12 (2008): 2884–2891, https://doi.org/10.1021/JE800678E/ASSET/IMAGES/LARGE/JE-2008-00678E_0001.JPEG.

48. K. Hayashi, Y. Nemoto, S. I. Tobishima, and J. I. Yamaki, "Mixed Solvent Electrolyte for High Voltage Lithium Metal Secondary Cells," *Electrochimica Acta* 44, no. 14 (1999): 2337–2344, https://doi.org/10.1016/S0013-4686(98)00374-0.

49. Y. Wang, "Wettability Enhanced by Electrolyte Additive to Boost the Electrochemical Performance of Lithium Metal Batteries," *Nano-Micro Letters* 13, no. 1 (2021): 210, https://doi.org/10.1007/S40820-021-00731-2.

50. P. Peljo and H. H. Girault, "Electrochemical Potential Window of Battery Electrolytes: The HOMO-LUMO Misconception," *Energy & Environmental Science* 11, no. 9 (2018): 2306–2309, https://doi.org/10.1039/c8ee01286e.

51. K. Kubota and H. Matsumoto, "Investigation of an Intermediate Temperature Molten Lithium Salt Based on Fluorosulfonyl(Trifluoromethylsulfonyl)Amide as a Solvent-Free Lithium Battery Electrolyte," *Journal of Physical Chemistry C* 117, no. 37 (2013): 18829–18836, https://doi.org/10.1021/jp405068q.

52. U. Pal, G. M. A. Girard, L. A. O'Dell, et al., "Improved Li-Ion Transport by DME Chelation in a Novel Ionic Liquid-Based Hybrid Electrolyte for Li-S Battery Application," *Journal of Physical Chemistry C* 122, no. 26 (2018): 14373–14382, https://doi.org/10.1021/acs.jpcc.8b03909.

53. X. Yin, X. Li, X. Cui, et al., "Molecular/Ionic Designs in the Electrolyte and Interphases for Lithium Metal Anode," *Batteries and Supercaps* 6 (2022): 202200394, https://doi.org/10.1002/batt.202200394.

54. P. Bai, J. Li, F. R. Brushett, and M. Z. Bazant, "Transition of Lithium Growth Mechanisms in Liquid Electrolytes," *Energy & Environmental Science* 9, no. 10 (2016): 3221–3229, https://doi.org/10.1039/c6ee01674j.

55. H. Liu, X. B. Cheng, R. Xu, et al., "Plating/Stripping Behavior of Actual Lithium Metal Anode," *Advanced Energy Materials* 9, no. 44 (2019): 1–7, https://doi.org/10.1002/aenm.201902254.

56. K. H. Chen, K. N. Wood, E. Kazyak, et al., "Mass Transport Effects on Voltage, Capacity, and Failure of Lithium Metal Anodes," *Journal of Materials Chemistry A* 5, no. 23 (2017): 11671–11681, https://doi.org/10.1039/c7ta00371d.

57. Y. Zhang, W. Luo, C. Wang, et al., "Low-Tortuosity, and Channel-Guided Lithium Metal Anode," *Proceedings of the National Academy of Sciences of the United States of America* 114 (2017): 3584–3589, https://doi.org/10.1073/pnas.1618871114.

58. X. B. Cheng, R. Zhang, C. Z. Zhao, F. Wei, J. G. Zhang, and Q. Zhang, "A Review of Solid Electrolyte Interphases on Lithium Metal Anode," *Advancement of Science* 3, no. 3 (2016): 1–20, https://doi.org/10.1002/advs.201500213.

59. A. M. Andersson, D. P. Abraham, R. Haasch, S. MacLaren, J. Liu, and K. Amine, "Surface Characterization of Electrodes from High Power Lithium-Ion Batteries," *Journal of The Electrochemical Society* 149 (2002): A1358–1369, https://doi.org/10.1149/1.1505636.

60. J. Alvarado, M. A. Schroeder, T. P. Pollard, et al., "Ether Electrolytes: A Pathway towards Lithium Metal Batteries with Ni-Rich Cathodes," *Energy & Environmental Science* 12, no. 2 (2019): 780–794, https://doi.org/10.1039/c8ee02601g.

61. B. Philippe, R. Dedryveire, M. Gorgoi, H. Rensmo, D. Gonbeau, and K. Edström, "Improved Performances of Nanosilicon Electrodes Using the Salt LiFSI: A Photoelectron Spectroscopy Study," *Journal of the*

American Chemical Society 135 (2013): 9829–9842, https://doi.org/10.1021/ja403082s.

62. L. E. Camacho-Forero and P. B. Balbuena, "Elucidating electrolyte decomposition under electron-rich environments at the lithium-metal anode," *Physical Chemistry Chemical Physics* 19, no. 45 (2017): 30861–30873, https://doi.org/10.1039/c7cp06485c.

63. Y. Lu, Y. Tian, Z. Xu, and H. Liu, "Interfacial Structures and Decomposition Reactions of Hybrid Anion-Based Ionic Liquids at Lithium Metal Surface from First-Principles and Ab Initio Molecular Dynamics," *Journal of Molecular Liquids* 366 (2022): 120232, https://doi.org/10.1016/j.molliq.2022.120232.

64. Y. Liu, P. Yu, Y. Wu, et al., "The DFT-ReaxFF Hybrid Reactive Dynamics Method with Application to the Reductive Decomposition Reaction of the TFSI and DOL Electrolyte at a Lithium-Metal Anode Surface," *Journal of Physical Chemistry Letters* 12, no. 4 (2021): 1300–1306, https://doi.org/10.1021/acs.jpclett.0c03720.

65. A. Wang, S. Kadam, H. Li, S. Shi, and Y. Qi, "Review on Modeling of the Anode Solid Electrolyte Interphase (SEI) for Lithium-Ion Batteries," *Npj Computational Materials* 4, no. 1 (2018): 15, https://doi.org/10.1038/s41524-018-0064-0.

Supporting Information

Additional supporting information can be found online in the Supporting Information section.